PCCP

Strain-driven surface reconstruction and cation segregation in layered Li(Ni1-x-yMnxCoy)O2 (NMC) cathode materials

Journal:	*Physical Chemistry Chemical Physics*
Manuscript ID	CP-ART-07-2020-003942.R2
Article Type:	Paper
Date Submitted by the Author:	12-Oct-2020
Complete List of Authors:	Garcia, Juan; Argonne National Laboratory Bareño, Javier; MIMSI Materials Chen, Guoying; Lawrence Berkeley National Laboratory, ESDR Croy, Jason; Argonne National Laboratory, Chemical Sciences and Engineering Iddir, Hakim; Argonne National Laboratory, Materials Division

ARTICLE

Strain-driven surface reconstruction and cation segregation in layered $Li(Ni_{1-x-y}Mn_xCo_y)O_2$ (NMC) cathode materials

Received 00th January 20xx,
Accepted 00th January 20xx

DOI: 10.1039/x0xx00000x

Juan C. Garcia[a], Javier Bareño[a,c], Guoying Chen[b], Jason R. Croy[a] and Hakim Iddir*[a]

The composition, structure and phase transformations occuring on cathode surfaces greatly affect the performance of Li-ion batteries. Li-ion diffusion and surface-electrolyte interaction are two major pheomena that impact the capacity and cell impedance. The effects of surface reconstruction (SR) of cathode materials on the peformance of Li-ion batteries are of current interest. However, the origin and evoluton of the SR are still not well understood. In this work, Density Functional Theory (DFT) calculations are used to investigate the processes taking place during surface segregation and reconstruction. Facet dependent segregation was found in $Li(Ni_{1-x-y}Mn_xCo_y)O_2$ (NMC) cathodes. Specifically, Co tends to segregate to the (104) surface of the primary particles within the transition metal layer, while Ni ions tend to segregate to the (012) surface in the Li layer, forming a SR. Experimental evidence shows the SR to be epitaxial with the bulk of the as-synthesized material, the new SR phase is pinned to the NMC unit cell leading to a strained SR. Here, we show that strain can stabilize a spinel structure of the SR layers. Understanding the effects of surface strain opens a new avenue for the design of cathode materials with enhanced surface properties.

1. Introduction

Lithium-ion batteries (LIBs) are the primary energy storage device for electric vehicles. However, there are still challenges to make this technology more competitive: improved safety, longer cycle life, fast charging and reduced price. To make any meaningful progress, a fundamental understanding of the processes taking place in these complex materials is necessary. For example, a deep understanding of the surface composition and structure is necessary in order to achieve better structural and chemical stability of the cathode as well as lower impedance and impedance rise with cycling.

Large variations in capacity, chemical and structural stability among different $Li(Ni_{1-x-y}Mn_xCo_y)O_2$ (NMC) compositions are well known and documented.[1–4] Local composition, particularly at surfaces, determine the nature of the active sites exposed to the electrolyte and additive molecules. Hence, affecting the evolution and nature of the surface reconstruction (SR) and cathode electrolyte interphases (CEI), and impacts the impedance and overall performance of the battery.[5–8]

The SR was shown to form, on both cycled and pristine layered oxide cathode compositions.[5,7,9–16] In particular, Lin et. al.[7] showed NMC undergoes a progressive reconstruction upon electrolyte exposure and subsequent cycling. The SR structure evolves from layered R-3m to rock salt Fm-3m, with the associated decrease in transition metal oxidation states due to O loss. The SR formation is inherent of layered oxides, given their intrinsic unstable surface terminations. Remarkably, Tasker type 3 surfaces[17] —alternating cation/anion surfaces with a dipole— are unstable. The present work focuses on the formation of a SR in pristine materials.

Oxide cathode surfaces are usually accompanied by not only structural changes, but compositional evolution as well. Yan et. al.[13] found a high concentration of Ni on the surface of as-synthesized $Li_{1.2}Ni_{0.2}Mn_{0.6}O_2$. Similarly, recent x-ray photo-electron spectroscopy (XPS) depth profiling experiments also showed Ni segregation to the surface.[18] It is proposed that, given the lower crystal field stabilization energy of Ni^{2+} compared to that of Co^{3+} and Mn^{4+}, Ni^{2+} would easily migrate and segregate to the surface. [18] Others,[14] found preferential elemental segregation of Ni to the (012) facets and Co to the (104) facets, along with evidence of SR formation on these facets, on as-synthesized Li- and Mn-rich (LMR) layered oxide particles. Facet dependent segregation has been attributed to the stabilization effect of transition metal terminated surfaces.[5] Note that the results from Li et al.[18] were based on XPS data performed on pellets and not on single particles as in Yan et al.[14]. Given the large surface area of (012) facets compared to (104) facets, higher overall Ni segregation to the surface can be expected.

Ni depletion of the bulk due to surface segregation has also been observed.[10] In general, the distribution of Ni is non-uniform with preference for grain boundaries and certain surface regions.[11] Transition metal (TM) cation migration into the Li layer can start from the surface of nanoparticles and extend to the inner region of the particle with the progression of the charge/discharge cycles.[12] Using high resolution Scanning

[a] Chemical Sciences and Engineering Division, Argonne National Laboratory, Lemont, Illinois 60439, United States.
[b] Energy Storage and Distributed Resources Division, Lawrence Berkeley National Laboratory, Berkeley, California 94720, United States.
[c] Currently at MIMSI Materials, Teknikringen 9, 583 30, Linköping, Sweden.
Electronic Supplementary Information (ESI) available: [details of any supplementary information available should be included here]. See DOI: 10.1039/x0xx00000x

Transmission Electron Microscopy (STEM) and Electron Energy Loss Spectroscopy (EELS) measurements on LMR materials, Boulineau et al.[19] observed surface spinel formation and further densification *via* transformation to disordered rock salt along with an increased Ni/Mn ratio near the surface layer. They attributed this surface Ni enrichment to Mn migration into the bulk layers accompanied by Ni and Mn migration into the Li layers as Li and O are removed from near the surface layers.[19]

The formation of Ni-rich SR layer seems to depend on synthesis conditions. Jarvis et.al.[20] observed a rock salt like SR Ni rich surfaces when synthesized at lower temperature and shorter times. They claimed that the NaCl-like structure at the surface might be composed of local spinel-like regions that average out in the 2-D projection. They concluded that Ni at the surface helps stabilize the NaCl-like structure, but more work is needed to fully understand the role of Ni in the SR layers.

Despite the fact that TM segregation and their deleterious effects have been observed in many studies, a consensus on the origin and thermodynamic driving force for such processes is still lacking. In this work, we propose a different mechanism that involves Ni migration into the Li layer and its preference to segregate to the surface, that eventually triggers spinel formation.[21] The actual driving force for Ni enrichment near the surface is hence a favorable Li-Ni exchange near the surface and not necessarily Mn migration away from the surface into the bulk, particularly considering that the spinel-like SR phase is also observed even in pristine non-cycled materials. Isotropic Mn segregation to the inner layers would not explain the observed anisotropic segregation of Ni to (012) and Co to (104) surfaces.

Herein, we introduce a facet-dependent TM segregation through a combined phase-change/segregation stabilized by the strain on the SR. First, we reiterate the stabilization effect of Co on the (104) surface. Second, we compare the formation of Li/Ni anti-site defects in different positions and configurations. Finally, we introduce the hypothesis of the strain induced stabilization of the SR, which to the best of our knowledge is the first time that strain has been proposed as a factor for the stabilization of the SR.

2. Methodology

The calculations were performed within the spin polarized density functional theory (DFT) methodology as implemented in the Vienna Ab Initio Simulation Package (VASP).[22,23] The generalized gradient approximation (GGA) is used to model the exchange-correlation potentials as developed by Perdew, Burke, and Ernzerholf (PBE).[24] The interaction between valence electrons and ion cores is described by the projected augmented wave (PAW) method.[25] Furthermore, the GGA+U scheme is used for applying the on-site correlation effects among 3d electrons of the transition metals, where the parameter of (U−J) is set to 5.96, 5.00, and 4.84 eV for Ni, Co, and Mn, respectively. [26] The magnetization was used to assign the oxidation state of the ions. Therefore, in order to get a better representation of the electronic structure, a single point calculation with a screened hybrid functional (HSE06) is performed after each geometry optimization.[27] It is important to highlight that the purpose of the final HSE06 single point calculations are solely to check that the geometry do not lead to spurious electronic structure effect and wrong oxidation states. Moreover, although HSE06 functional might give slightly different equilibrium cell size, the energy trend found with DFT+U is the same. Given the computational cost of a geometry relaxation using HSE06, a compromise between a reasonable geometry at the DFT+U level and a reasonable electronic structure has been adopted. The authors have reported this procedure before. [26,28–32] Previous work by other authors have used a similar procedure. For instance, Das et. al.[33] cross-checked their DFT+U calculations using HSE screened Coulomb hybrid density functional wherever they felt necessary. In this latest reference, the trends were found to be the same between the DFT+U and HSE06 for Ni_3O_4 phases. Previous work[34] has shown that the HSE calculated migration barrier differs from GGA by about 10%. Others have used the same argument to justify the calculation at the GGA level.[35] Furthermore, the difference in volume for $LiNiO_2$ computed at the DFT+U level and HSE06 has been reported to be ~2% for the fully lithiated and 0% when delhitiated.[36] Hence, the change in lattice parameters would be even smaller. All these arguments justify the use of DFT+U for the geometry relaxion.

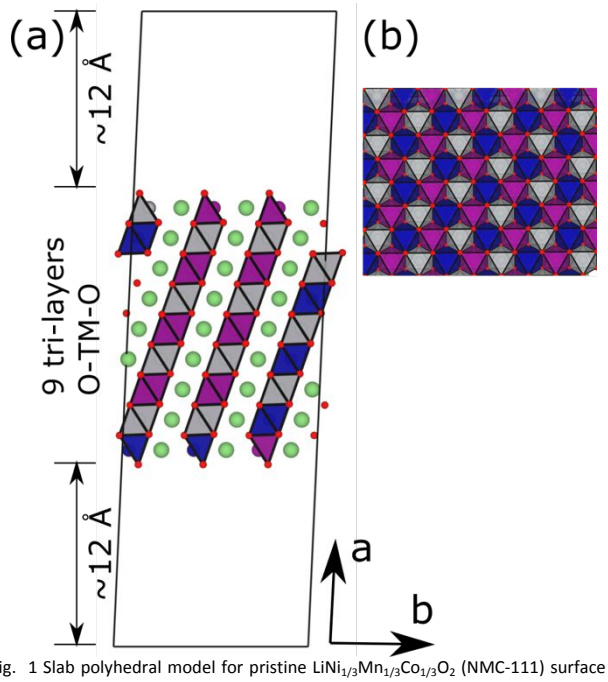

Fig. 1 Slab polyhedral model for pristine $LiNi_{1/3}Mn_{1/3}Co_{1/3}O_2$ (NMC-111) surface (012) without cation disorder. (a) Slab model where the periodic box is indicated by the solid black line. Arrows marked a, b and c represent the direction of the lattice vectors. (b) Distribution of transition metal cations in their respective layers. The NiO_6 octahedra are represented in grey, CoO_6 octahedra are represented in blue and MnO_6 octahedra are represented in purple. The Li ions are indicated by green spheres.

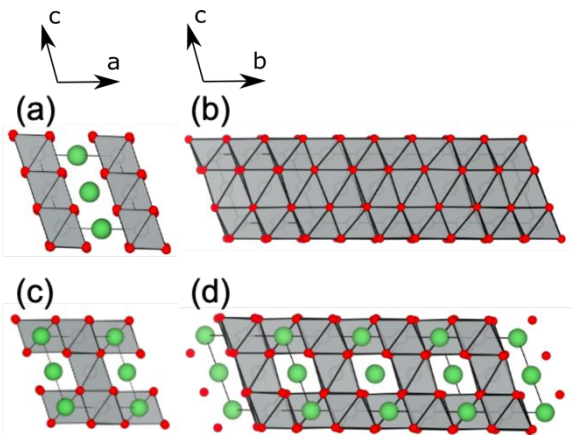

Fig. 2 Polyhedral model for pristine bulk $LiNiO_2$ rotated to get the (012) plane perpendicular to c-direction of the super-cell. (a-b) layered structure and (c-d) over-lithiated spinel structure. The NiO_6 octahedra are represented in grey while Li ions are indicated by green spheres.

All surface calculations were performed using a periodically repeating slab separated by ~24 Å vacuum along the surface normal. For instance, Fig. 1 shows the polyhedral representation of the (012) surface slab for the NMC-111 composition. The slab is composed of 324 atoms arranged in nine layers perpendicular to the surface. The configuration of cations in the TM layer was determined in a previous work.[26] An index notation based on the hexagonal unit cell of the unreconstructed layered structure is used. The (104) and (102) facets are used as prototype surfaces since previous work has determined those facets as being the most predominant and active toward oxygen loss in primary NMC particles.[26] The surface energy is defined as the difference in the free energy between the bulk material and a model slab surface per unit area (γ). We also assume the entropic and volumetric contributions to be negligible. The vibrational entropy is known to be negligible.[37,38] The configurational entropy contribution of Ni segregation from bulk NMC-111 (1/6 of sites occupied by Ni) to the extreme case of $LiNiO_2$ surface composition (1/2 of the sites occupied by Ni) is -2.5*10-5 eV/K according to the regular solution model (see SI for calculation details), which is orders of magnitude smaller than the thermal contribution.[39]

Since it is not possible to apply strain to a surface in a slab, a special super cell was built to account for the effect of stresses on phase transformations at the surfaces. The goal in building this special cell is twofold: first, to be able to apply tensile and compressive stress in the right crystallographic directions, and second to accommodate layered and spinel-like structures in the same cell. For instance, a bulk super-cell was rotated such that the (012) plane becomes the top facet of the supercell. Fig. 2 shows a polyhedral representation of the modified cell. The lattice vector "a" goes through the Li-Ni nearest neighbors, the "b" lattice vector goes through the Li-Ni second nearest neighbors and the "c" lattice vector goes through a Li-Li nearest neighbors forming the smallest angle with the perpendicular to the ab plane. The modified cell has 48 ions, which makes it suitable for extensive calculations at several applied strain values. The cell can be strained in any of the directions given by the lattice vectors. Since the final objective is to emulate the behavior of a thin film pinned to the core material, the a and b direction were changed to account for tensile and compressive strain up to 10% with respect to the fully relaxed cell. In all the calculations the c direction was allowed to relax to its equilibrium position. A similar procedure was applied for the (104) surface.

To obtain and image a particle surface, $LiNi_{0.5}Mn_{0.3}Co_{0.2}O_2$ (NMC532) crystal sample was prepared via a two-step process: preparation of transition-metal hydroxide precursors by the coprecipitation method followed by annealing them with lithium hydroxide. The synthesis procedure was described in detail in a previous publication.[16] Aberration-corrected scanning transmission electron microscopy (AC-STEM) was performed using a JEOL JEM-ARM200CF STEM equipped with a cold field emission gun with 0.78 Å spatial resolution. The atomic resolution image was obtained by a high-angle annular dark-field (HAADF) detector with a 90 mrad inner-detector angle and a 22 mrad probe convergence angle.

3. Results and Discussions

3.1 Elemental segregation within the transition metal layer

To provide a fundamental understanding of the preferential elemental segregation observations mentioned above, a (104) surface slab for $Li(Ni_{1-x-y}Mn_xCo_y)O_2$ with composition x = y = 1/3 (NMC-111) was built and the Co concentration on the surface was varied in different simulations by swapping Co atoms from the bulk to the surface, keeping the overall supercell stoichiometry constant. The symmetric slab model representing the (104) facet consists of 384 ions distributed in 9 layers. Each layer is stoichiometric, resulting in a non-polar surface. Fig. 3 shows a schematic of the (104) surface layer. The octahedron formed by the metals and Li atoms with the surrounding O atoms in the central layer were kept fixed to mimic the bulk of the material. Fig. 3a represents the surface layer unit cell for the stoichiometric slab. Fig. 3b and 3c show the surface of the slab with an excess content of Co ions of one and two extra Co per surface layer, respectively. Note that we have three Co atoms per surface layer for the stoichiometric NMC-111 reference supercell.

The surface energy decreases with increasing Co concentration at the surface. The driving force for the preferential segregation of Co to the (104) surface can be

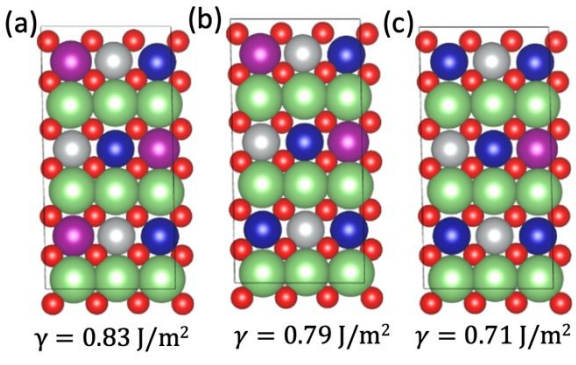

Fig. 3. Schematic representation of the slab model for NMC-111 (104) top surface layer with (a) stoichiometric amount of Co, (b) excess of one Co ion per surface, (c) excess of two Co ions per surface. Small red sphere represents oxygen, green, grey, purple and blue spheres represent Li, Ni, Mn and Co respectively. The surface energy (γ) is indicated for each model.

explained by the change in coordination of the Co ions at the surface. The formation of the (104) surface implies cleavage of the axial Co-O bond, which changes the Co coordination from octahedral to square pyramidal. It has been demonstrated previously[26,40] that Co in the square pyramidal configuration prefers an intermediate spin state because the crystal field splitting energy is lower than the spin pairing energy. This configuration leads to d_{xy} and $d_{x^2-y^2}$ orbitals with lower energy.

Cobalt within the TM layer shows a driving force for segregation towards the surface. On the other hand, Ni within the TM layer does not show any driving force for Ni to segregate to the surface. The total energy of the system increases with the increase of Ni within the top three TM surface layers. In fact, slabs with non-uniform Ni concentration profiles are energetically unfavorable. Although the supercell models used here are large (9 TM layers, 384 atoms), such segregated slabs cannot represent actual systems accurately, given the strain produced in the cell due to the constant overall stoichiometry constraint.

3.2 Ni segregation via the Li layer

Since there is no evidence of a driving force for the segregation of Ni within the transition metal layer, a different mechanism must be responsible for the experimentally observed Ni rich surfaces. Ni is known to produce Li-Ni anti-site defects. Such defects can actually migrate to the surface given the mobility of Ni^{2+} ions which have a similar size to Li ions. In fact, it has been shown that Ni can readily diffuse to the surface once it is in the Li layer given the lower energy barrier for Ni diffusion in the Li layer compared to that of Li.[5] In order to get some insights into this process, we computed the energy of formation of Li-Ni anti-site defects in the bulk of NMC-111 to be E_f = 0.3eV/f.u. Given the energy of formation, the concentration (C) of a defect can be estimated as: $C = Aexp(-Ef/k_BT)$. Where the pre-exponential factor accounts for the total number of defect configurations, kB is the Boltzmann constant and T is the temperature. [41] Such energy of formation corresponds to a concentration of about 1.3%. This value is in agreement with experimental values (1.6%) for NMC-111.[42] Our results show that the probability of a single Ni antisite defect formation is insensitive to its distance to the surface. A schematic of the Ni antisite location is shown in Fig. S1.

As expected, the energy of formation of Ni antisite defects increases with the concentration. However, the behavior is reversed for a line defect configuration. The energy to form a line defect along the b-direction (three aligned defects given the cell considered in this work due to the periodic boundary conditions) is smaller than the energy to form two defects (discontinuous line defect). The dark blue bars in Fig. 4 show the energy of formation of a single, double or line defect in the bulk. The formation energy of these defects is higher for the pair configuration. The formation energy of a line defect in the bulk, although lower than the pair defect, remains positive (low concentration expected). However, when we consider the formation of such defects near the top surface layers (shown in light blue in Fig. 4), the energy of formation of a line defect becomes negative (thermodynamically favorable, higher concentration expected). The special configuration of the line defect decreases the total energy in spite of the increased concentration of defects. Furthermore, the overall favorable formation of Li-Ni exchange (line defect) near the surface layers is in fact a result of energy gain near the surface and energy cost for creating a different bulk stoichiometry (Ni-poor, given our cell size). This suggests that the energy gain from higher Li-Ni exchange at the surface should be even higher than the reported values here. Larger supercells with more bulk-like layers capable to simulate real system sizes that can compensate change in stoichiometry are needed to reach the absolute values.

There may be several factors contributing to the stability of Li/Ni antisite line defects. The formation of a Li/Ni antisite defect produces a dipole (two domain walls). However, in the case of line defect configurations, the overall electric field cancels out because the dipoles are oriented in a spiral in the direction of the rows. In this case the energy cost of domain walls is eliminated, hence contributing to the stabilization of such extended defect configurations. The proximity of the line defect to the surface also allows for better dissipation of strain resulting from the local distortions around the Li-Ni exchange sites. At the extreme case (high Ni content compositions and/or cycled cathodes), as the number of Ni antisite defects increases near the surface, an over-lithiated $Li_2Ni_2O_4$ spinel-like phase forms (for pristine compositions). This phase could explain the formation of the Ni-rich SR observed experimentally.[14] For such extended reconstructions, the stabilization effect can be understood also as a phase transformation which could be stabilized by two effects, namely, the strain induced at the interface and the relaxation in the direction perpendicular to the surface. Lower lithiated versions of this SR would form for cycled cathodes, as a result of Li and O loss. The thermodynamic stability of Li and O poor phases (rock salt like) compared with layered has been demonstrated before.[7]

For NMC the spinel is not the most stable phase. However, the SR, usually referred to as 'spinel-like' can in fact adopt a spinel structure, with composition change. The TEM images in Fig. 5 show that the SR is indeed epitaxial to the bulk. However,

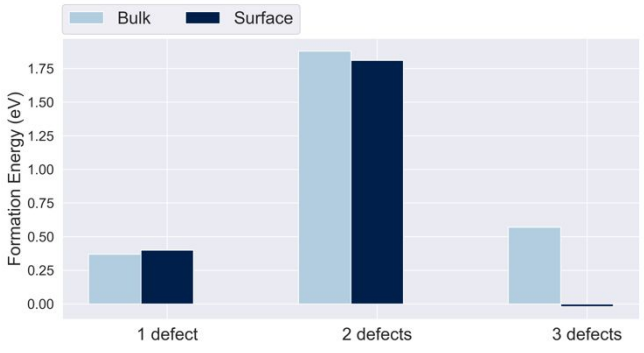

Fig. 4 Li/Ni antisite defect formation energy change with the number of defects. The defects are located in the same layer forming a single (1 defect), a double (2 defects) and a row of continuous defects (3 defects).

the new spinel-like phase within the SR has a different equilibrium unit cell compared to the bulk NMC phase. A

coherent interface is possible for this system because the lattice misfit is less than 10%.[43] Furthermore, according to Bhattacharyya and Maurice:[43] "The lattice misfit may contribute significantly to the stresses in films if the thickness is of submicron scale". Hence, the SR is strained because it is pinned to the bulk unit cell. Since the SR is very thin, the direction perpendicular to the surface allows for the ions to relax and release some of the extra elastic energy due to the strain. Indeed, the elastic energy (E_H) is proportional to the thickness of the SR (h) layer according to the expression:

$$E_H = Bhf_m^2$$

Where B is the elastic modulus and f_m is the misfit parameter (lattice mismatch). Previous work has shown that epitaxially constrained spinel phases go through a topotactic reaction characterized by the redistribution of metal ions while preserving the O-sublattice structure.[44] The epitaxial constraint is achieved using a thin film approach that is analogous to the SR layer pinned to a bulk material acting as a substrate.

In practice, the boundary between the SR and the "perfect" layered phase is not sharp. A gradient in the amount of Ni in the Li layer from the SR to the bulk of the particle is usually observed.[16] The existence of such a buffer layer is evidence for the presence of strain/composition gradient between the surface and the bulk. In order to model such a system using DFT, a heterogeneous slab is needed: two different unit cells (spinel and layered) have to be matched on top of each other in the corresponding direction. Since the unit cell size of spinel and layered phase are different, the corresponding slab needed would be too large and not suitable for DFT calculations. Instead, we strain a bulk phase with the crystal structure of the SR layer, consistent with strain imposed by the cube-on-cube epitaxy with the bulk, allowing for relaxation perpendicular to the facet of interest.

Since a Ni rich SR has been found experimentally, we will start our analysis considering the extreme case of complete Ni segregation to the (012) surface of fully lithiated NMC-111. In particular, we consider the relative stabilities of the possible $Li_2Ni_2O_4$ (over-lithiated spinel) and $LiNiO_2$ (layered) surface phases. Fig. 6 shows the total energy of the system when pinned to the (012) facet of NMC-111 as a function of the C/C_0. The parameter C_0 represents the unstrained reference SR phase (see schematic in Fig. S2). In the unrelaxed system, where C/C_0 equals 1.00, the strain caused by pinning the SR phase to the NMC unit cell increases the energy of the $Li_2Ni_2O_4$ SR phase (S-LNO/NMC, Fig. 6a) over the layered phase (L-LNO/NMC), which is slightly more stable at this point.

However, if the SR is considered as a thin film that is allowed to relax in the direction perpendicular to the surface, the surface film would shrink in response to the applied tensile strain. The energy would then decrease, and the spinel phase would be more stable than the layered. However, for pure $Li_2Co_2O_4$ the result is opposite, and the total energy of the layered phase is always lower than that of the spinel phase (see Fig. 6b).

In general, the strain induced stabilization effect is intensified upon delithiation of the spinel phase (SR layers). Fig. 7 shows the effect of strain on $LiNi_2O_4$ ($Li_{0.5}NiO_2$). The circle, square and triangle marks represent the layered, spinel-like and

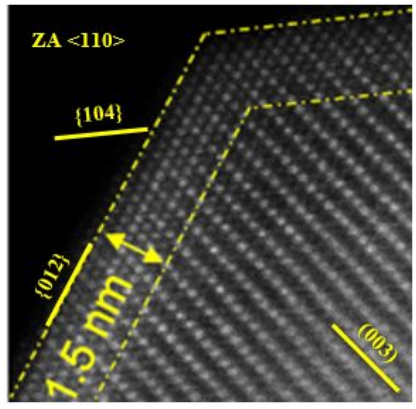

Fig. 5. A STEM image shows an area of a primary NMC particle close to a corner between a {012} facet and a {104} facet. The bulk region of the NMC particle (lower-right area of the micrograph) clearly shows the characteristic (003) of the layered NMC structure. Close to the facets, a SR layer approximately 1.5 nm deep is evident. Transition metal migration to Li planes in the SR results in local spinel symmetry.

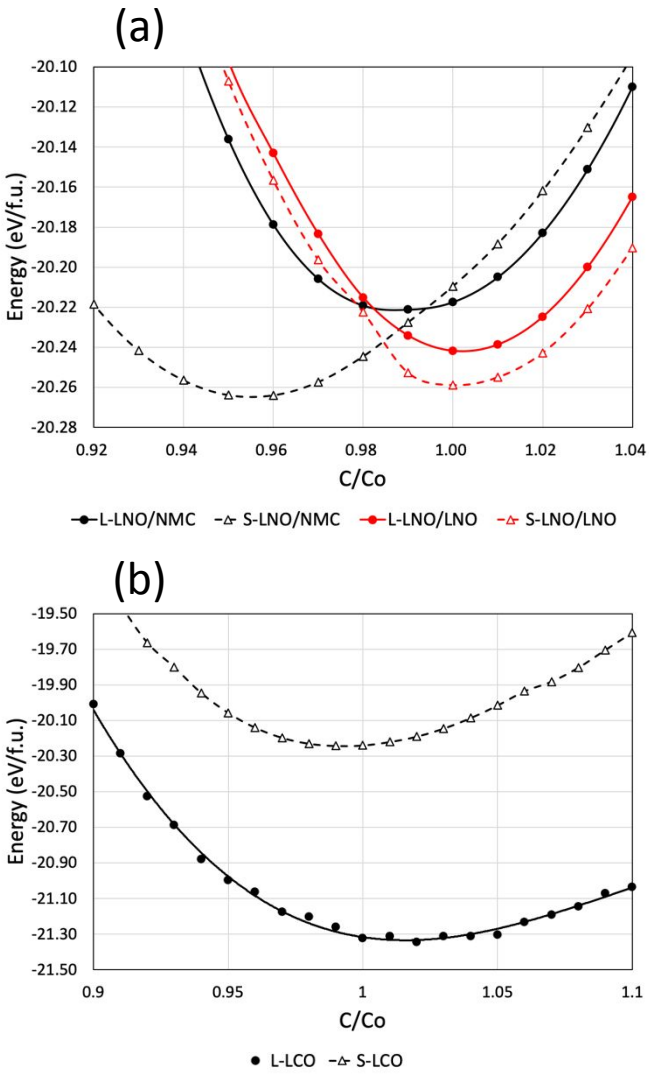

Fig. 6. Energy change with c direction expansion for (a) layered and overlithiated spinel $LiNiO_2$ ($Li_2Ni_2O_4$) pinned to NMC-111 and layered $LiNiO_2$, (b) layered and overlithiated spinel $LiCoO_2$ ($Li_2Co_2O_4$) pinned to NMC-111 (012) surface.

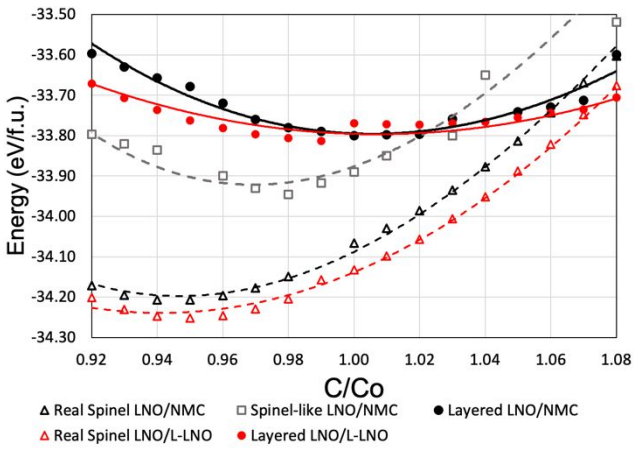

Fig. 7. Energy change with expansion/contraction in the c direction for layered, spinel-like and real spinel $LiNi_2O_4$ pinned to the (012) facets of NMC-111 (black-grey) and pinned to LNO (red).

spinel $LiNi_2O_4$ pinned to NMC-111 lattice, respectively. As expected, since the layered $LiNi_2O_4$ and layered NMC-111 are isomorphic, the effect of strain is small (black circles in fig. 7), and the minimum energy is found at a value of C/Co equal to 1.10, indicating a slightly expanded SR. However, for the spinel-like phase pinned to NMC-111 (black squares in fig. 7), the minimum energy is found at a value of C/Co equal 0.98, indicating a reduction in thickness of the SR layer after formation. Furthermore, the equilibrium energy decreases compared to the layered phase, indicating a driving force for the phase transformation. The effect is more pronounced for the transformation to a real spinel phase (black triangles in fig. 7), with Li being in the most stable tetrahedral sites. Hence, the strain-driven stabilization is exacerbated when there is Li loss at the surface and the spinel phase is favored near the top SR layers. In the delithiated case ($Li_{0.5}NiO_2$) the driving force for the phase change is -0.45eV/f.u. compared with -0.04eV/f.u. (Fig. 6a) for the fully lithiated surface. It is important to notice that there is more noise in the data for $LiNi_2O_4$ (spinel-like) compared to $LiNiO_2$ and spinel $LiNi_2O_4$. This effect is due to the increased number of possible configurations in the Li layer upon delithiation.

It can be hypothesized that upon delithiation there is a driving force to form a spinel phase at the surface which would remain stable after re-lithiation. This result would certainly explain not only the continuous phase transformation of the SR from overlithiated spinel to spinel, and the SR thickness increase with cycling, but also the commonly observed tendency for Li loss from the surface layers.

The strain-driven Ni segregation to the surface of NMC particles and the associated formation of spinel-like structures of the SR layer, does not seem to favorable for pure $LiNiO_2$ compositions, i.e. $Li_2Ni_2O_4$ on $LiNiO_2$. In this case, although there is a small driving force for Li-Ni exchange on the top atomic layer only, and spinel formation, there is no strain-driven surface structure/composition reconstruction (see Fig. 6a red curves). The energy difference between the layered and spinel-like structure is very small, essentially degenerate, consistent with previous calculations.[33] The SR layer observed (reduced Ni on the surface) on pristine $LiNiO_2$ samples may be, in general, due to the propensity for Li loss and Ni^{2+} formation during synthesis, particularly if conditions are not carefully optimized, even in the presence of excess Li.[45] In fact, for the $LiNi_2O_4$ (50% less Li, i.e.$Li_{0.5}NiO_2$) pinned to the pristine $LiNiO_2$ the total energy decreases (by 0.45 eV/f.u.) when the real spinel phase is formed and the SR shrinks up to 4% (see red curves in Fig. 7).

4. Conclusions

In summary, a complex mechanism for Ni segregation is put forward, where we show the presence of a thermodynamic driving force for the segregation of Ni to the surface via Li-Ni exchange near the (012) surface, and strain-driven stabilization of the $LiNi_2O_4$ spinel thin film pinned to NMC and $LiNiO_2$ lattices. This is an indication of a driving force for the inter-dependence of Ni segregation and surface reconstruction in the (012) facet. The elemental segregation and SR layer formation are intimately linked and facet dependent phenomena. The global composition and strain affect the nature and the thickness of the SR, which impacts the impedance and also necessarily the chemical stability of the cathode/electrolyte interface as well.

Conflicts of interest

There are no conflicts to declare.

Acknowledgements

We gratefully acknowledge support from the U. S. Department of Energy (DOE), Office of Energy Efficiency and Renewable Energy, Vehicle Technologies Office. Argonne National Laboratory is operated for DOE Office of Science by UChicago Argonne, LLC, under contract number DE-AC02-06CH11357. We acknowledge the computing resources provided on Bebop; a high-performance computing cluster operated by the Laboratory Computing Resource Center (LCRC) at Argonne National Laboratory. This research also used resources of the National Energy Research Scientific Computing Center (NERSC), a U.S. Department of Energy Office of Science User Facility operated under Contract No. DE-AC02-05CH11231.

References

1 J. Cho, H. Jung, Y. Park, G. Kim and H. S. Lim, *J. Electrochem. Soc.*, 2000, **147**, 15–20.
2 J. Xu, F. Lin, M. M. Doeff and W. Tong, *J. Mater. Chem. A*, 2017, **5**, 874–901.
3 S.-K. Jung, H. Gwon, J. Hong, K.-Y. Park, D.-H. Seo, H. Kim, J. Hyun, W. Yang and K. Kang, *Adv. Energy Mater.*, 2014, **4**, 1300787.
4 H. Sun and K. Zhao, *J. Phys. Chem. C*, 2017, **121**, 6002–6010.
5 M. Gu, I. Belharouak, A. Genc, Z. Wang, D. Wang, K. Amine, F.

Gao, G. Zhou, S. Thevuthasan, D. R. Baer, J.-G. Zhang, N. D. Browning, J. Liu and C. Wang, *Nano Lett.*, 2012, **12**, 5186–5191.
6 H. Zhang, B. M. May, J. Serrano-Sevillano, M. Casas-Cabanas, J. Cabana, C. Wang and G. Zhou, *Chem. Mater.*, 2018, **30**, 692–699.
7 F. Lin, I. M. Markus, D. Nordlund, T.-C. Weng, M. D. Asta, H. L. Xin and M. M. Doeff, *Nat Commun*, 2014, **5**, 3529.
8 K. Kang, Y. S. Meng, J. Bréger, C. P. Grey and G. Ceder, *Science*, 2006, **311**, 977–980.
9 B. Xu, C. R. Fell, M. Chi and Y. S. Meng, *Energy Environ. Sci.*, 2011, **4**, 2223–2233.
10 P. Yan, A. Nie, J. Zheng, Y. Zhou, D. Lu, X. Zhang, R. Xu, I. Belharouak, X. Zu, J. Xiao, K. Amine, J. Liu, F. Gao, R. Shahbazian-Yassar, J.-G. Zhang and C.-M. Wang, *Nano Lett.*, 2015, **15**, 514–522.
11 M. Gu, A. Genc, I. Belharouak, D. Wang, K. Amine, S. Thevuthasan, D. R. Baer, J.-G. Zhang, N. D. Browning, J. Liu and C. Wang, *Chem. Mater.*, 2013, **25**, 2319–2326.
12 M. Gu, I. Belharouak, J. Zheng, H. Wu, J. Xiao, A. Genc, K. Amine, S. Thevuthasan, D. R. Baer, J.-G. Zhang, N. D. Browning, J. Liu and C. Wang, *ACS Nano*, 2013, **7**, 760–767.
13 P. Yan, J. Zheng, D. Lv, Y. Wei, J. Zheng, Z. Wang, S. Kuppan, J. Yu, L. Luo, D. Edwards, M. Olszta, K. Amine, J. Liu, J. Xiao, F. Pan, G. Chen, J.-G. Zhang and C.-M. Wang, *Chem. Mater.*, 2015, **27**, 5393–5401.
14 P. Yan, J. Zheng, J. Zheng, Z. Wang, G. Teng, S. Kuppan, J. Xiao, G. Chen, F. Pan, J.-G. Zhang and C.-M. Wang, *Adv. Energy Mater.*, 2016, **6**, n/a-n/a.
15 Q. Lin, W. Guan, J. Meng, W. Huang, X. Wei, Y. Zeng, J. Li and Z. Zhang, *Nano Energy*, 2018, **54**, 313–321.
16 J. Zhu, S. Sharifi-Asl, J. C. Garcia, H. H. Iddir, J. R. Croy, R. Shahbazian-Yassar and G. Chen, *ACS Appl. Energy Mater.*, 2020, **3**, 4799–4811.
17 P. W. Tasker, *J. Phys. C: Solid State Phys.*, 1979, **12**, 4977.
18 G. Li, Q. Li, L. Li, J. Fan, Q. Ge, D. Xie, J. Zheng and G. Li, *Appl. Surf. Sci.*, 2018, **427**, 226–232.
19 A. Boulineau, L. Simonin, J.-F. Colin, C. Bourbon and S. Patoux, *Nano Lett.*, 2013, **13**, 3857–3863.
20 K. Jarvis, C.-C. Wang, M. Varela, R. R. Unocic, A. Manthiram and P. J. Ferreira, *Chem. Mater.*, 2017, **29**, 7668–7674.
21 Vehicle Technologies Office Merit Review 2018, https://www.energy.gov/eere/vehicles/downloads/vehicle-technologies-office-merit-review-2018-enabling-high-energy-high-0.
22 G. Kresse and J. Furthmüller, *Comp. Mater. Sci.*, 1996, **6**, 15–50.
23 G. Kresse and J. Hafner, *Phys. Rev. B*, 1993, **47**, 558–561.
24 J. P. Perdew, K. Burke and M. Ernzerhof, *Phys. Rev. Lett.*, 1996, **77**, 3865–3868.
25 P. E. Blöchl, *Phys. Rev. B*, 1994, **50**, 17953–17979.
26 J. C. Garcia, J. Bareño, J. Yan, G. Chen, A. Hauser, J. R. Croy and H. Iddir, *J. Phys. Chem. C*, 2017, **121**, 8290–8299.
27 A. V. Krukau, O. A. Vydrov, A. F. Izmaylov and G. E. Scuseria, *The J. Chem. Phys.*, 2006, **125**, 224106.
28 C. Peebles, J. Garcia, A. P. Tornheim, R. Sahore, J. Bareño, C. Liao, I. A. Shkrob, H. H. Iddir and D. P. Abraham, *J. Phys. Chem. C*, , DOI:10.1021/acs.jpcc.8b02056.
29 A. Tornheim, J. C. Garcia, R. Sahore, H. Iddir, I. Bloom and Z. Zhang, *J. Electrochem. Soc.*, 2019, **166**, A440–A447.
30 A. Tornheim, S. Sharifi-Asl, J. C. Garcia, J. Bareño, H. Iddir, R. Shahbazian-Yassar and Z. Zhang, *Nano Energy*, 2019, **55**, 216–225.
31 B. Han, B. Key, S. H. Lapidus, J. C. Garcia, H. Iddir, J. T. Vaughey and F. Dogan, *ACS Appl. Mater. Interfaces*, , DOI:10.1021/acsami.7b13597.
32 J. R. Croy, J. C. Garcia, H. Iddir, S. E. Trask and M. Balasubramanian, *J. Power Sources*, 2020, 228335.
33 H. Das, A. Urban, W. Huang and G. Ceder, *Chem. Mater.*, 2017, **29**, 7840–7851.
34 M.-J. Zheng, N. Swaminathan, D. Morgan and I. Szlufarska, *Phys. Rev. B*, 2013, **88**, 054105.
35 S. Xu, R. M. Jacobs, H. M. Nguyen, S. Hao, M. Mahanthappa, C. Wolverton and D. Morgan, *J. Mater. Chem. A*, 2015, **3**, 17248–17272.
36 V. L. Chevrier, S. P. Ong, R. Armiento, M. K. Y. Chan and G. Ceder, *Phys. Rev. B*, 2010, **82**, 075122.
37 P. Masri, P. W. Tasker, J. P. Hoare and J. H. Harding, *Surf. Science*, 1986, **173**, 439–454.
38 A. Ferrari and F. Körmann, *Appl. Surf. Sci.*, 2020, **533**, 147471.
39 R. A. Van Santen and M. A. M. Boersma, *J. Catalysis*, 1974, **34**, 13–18.
40 D. Qian, Y. Hinuma, H. Chen, L.-S. Du, K. J. Carroll, G. Ceder, C. P. Grey and Y. S. Meng, *J. Am. Chem. Soc.*, 2012, **134**, 6096–6099.
41 G. H. Vineyard and G. J. Dienes, *Phys. Rev.*, 1954, **93**, 265–268.
42 Y. Xiao, T. Liu, J. Liu, L. He, J. Chen, J. Zhang, P. Luo, H. Lu, R. Wang, W. Zhu, Z. Hu, G. Teng, C. Xin, J. Zheng, T. Liang, F. Wang, Y. Chen, Q. Huang, F. Pan and H. Chen, *Nano Energy*, 2018, **49**, 77–85.
43 A. Bhattacharyya and D. Maurice, *Surf. Interfaces*, 2018, **12**, 86–94.
44 X. Chen, M. Vörös, J. C. Garcia, T. T. Fister, D. B. Buchholz, J. Franklin, Y. Du, T. Droubay, Z. Feng, H. Iddir, L. A. Curtiss, M. J. Bedzyk and P. Fenter, *ACS Appl. Energy Mater.*, , DOI:10.1021/acsaem.8b00270.
45 J. Xu, F. Lin, D. Nordlund, E. J. Crumlin, F. Wang, J. Bai, M. M. Doeff and W. Tong, *Chem. Commun.*, 2016, **52**, 4239–4242.